Characterizing the tumor microenvironment of metastatic ovarian cancer by single cell transcriptomics

Susan Olalekan[1*], Bingqing Xie[1], Rebecca Back[1], Heather Eckart[1], Anindita Basu[1,2*]

1 Department of Medicine, University of Chicago
2 Center for Nanoscale Materials, Argonne National Laboratory

*Correspondence: Anindita Basu (onibasu@uchicago.edu), Susan Olalekan (solalekan@uchicago.edu)

Abstract

Epithelial ovarian cancer is a highly heterogenous disease with a common metastatic site, the omentum. The presence of $CD8^+$T cells within the tumor is associated with overall survival however not every patient responds to checkpoint immune blockade aimed at restoring T cell function. Determining if a patient has T cells that respond to immunotherapies, their characteristics and how they can be manipulated to target cancer cells is an area of intense investigation in cancer therapy. The objective of this study was to determine the cellular composition and their transcriptional state in metastatic ovarian cancer samples using single cell RNA sequencing (scRNA-seq). Hierarchical clustering stratified our patient cohort into 2 main groups: a high T cell and 2) a high monocyte signature group suggesting differences in immune response. To assess the immune response in these patient samples, we performed an unsupervised clustering of the T cell population in the two groups. The T cell population clustered into 4 and 3 subpopulations in the high T cell and high monocyte group respectively. A granulysin expressing T cell population was unique to the High T cell group. Interestingly, although both groups had resident memory $CD8^+$T ($CD8^+$Trm) cells, only the $CD8^+$Trm cells in the high T cell group expressed TOX, a recently described transcription factor. TOX confers longevity to T cells within immunosuppressive environment such as cancer. Along with TOX^+ T cells we found unique B cells and other novel macrophage clusters in our high T cell response group. In conclusion, our scRNA-seq data reveal novel subsets of immune cells that may contribute to the success of immunotherapy in ovarian cancer patients.

Introduction

Ovarian cancer is the most lethal malignancy of the female reproductive tract[1]. Conventional therapy involving cytoreductive surgery and chemotherapy are 90% effective when cancer is diagnosed at the early stage when it is still restricted to one or both ovaries. Unfortunately, most ovarian cancer cases are diagnosed at stage III when the cancer has metastasized and the diagnosis in these patients result in a 30% 5-year survival rate[2]. Additionally, the efficacy of novel therapies such as immunotherapy is not consistent among cancer patients. We therefore need biomarkers for early clinical detection and that are predictive of patient response to novel therapies. Furthermore, to develop efficacious therapies for metastatic ovarian cancer, we need to define the cellular heterogeneity and the transcriptional state within the tumor microenvironment. Immunohistochemical staining and flow cytometry have been useful in categorizing the cell types based on specific cell surface markers. However, cell classification solely on the basis of phenotypic markers masks the heterogeneity within individual cell types. Bulk profiling studies average gene expression and fail to identify the respective contribution of cell subsets. Alternatively, single cell RNA sequencing (scRNA-seq) has emerged a powerful tool to interrogate tumor composition revealing previously uncharacterized cellular heterogeneity as well as revealing gene regulatory networks within the tumor microenvironment[3-8].

Although epithelial ovarian is a highly heterogenous disease, all histotypes commonly metastasize to the omentum. The omentum is mainly an adipose tissue in the peritoneal cavity containing aggregates of immune cells in areas called milky spots. These milky spots act similar to lymph nodes, collecting and responding to antigen within the peritoneal cavity. Interestingly, ovarian cancer cells preferentially colonize adipose tissue with milky spots in the peritoneal cavity[9]. Additionally, adipocytes provide adipokines and act as a source of energy for ovarian cancer cells[10]. It is likely that integrated signals from adipocytes and immune cells make the omentum a focal point of metastasis of ovarian cancer. In high grade serous ovarian carcinoma, the most common histotype, the presence of tumor infiltrating lymphocytes is associated with significantly longer overall survival suggesting that not all immune cells encourage metastasis of ovarian cancer[11]. In this current study, we use scRNA-seq technology to examine the cells within omental tumors from 6 patients with different histotypes of ovarian cancer. We identified 12 cell clusters including epithelial and stromal populations. Patients were divided into two groups based on immune signatures; 1) T cell response 2) monocyte response group. This unprecedented concurrent transcriptomic analysis of all cells within metastatic ovarian cancer unravels patient specific response to cancer and highlights patients suitable for cancer immunotherapy.

Materials and methods

Tissue collection

130 Ovarian cancer tissue was collected from women undergoing debulking surgery at the University
131 of Chicago. Human tissue acquisition after patient deidentification was approved by the
132 university of Chicago institutional review board for human research. Ovarian cancer tissue was
133 histologically carcinoma classified and staged by a pathologist according to tumor-node-
134 metastasis (TMN) and/or international federation of gynecology and obstetrics (FIGO)
135 classifications (Table 1). Three of the ovarian cancer samples originated from the left fallopian
136 tube (with associated serous tubal intraepithelial carcinoma (STIC)).
137
138 **Immunohistochemistry**
139
140 Tissue sections were fixed overnight in 4% formaldehyde at 4^0C. After serial dehydration, the
141 tissues were embedded in paraffin and cut into 5μm thick sections. Histological evaluation was
142 done with hematoxylin and eosin (H&E). Immunohistochemical staining was performed to
143 confirm the presence of cytokeratin-7 (Thermofisher), pan-vimentin (DAKO), CD45 (Agilent
144 Technologies), CD3 (Human envision) and CD19 cells. Briefly, sections were deparaffinized and
145 rehydrated through xylenes and serial dilutions of EtOH to distilled water. Tissue sections were
146 incubated in citrate buffer, pH 6 and heated in a microwave oven. Anti-cytokeratin-7(1:1000),
147 anti-Vimentin (1:100), anti-CD45 (1:100), anti-CD3 (1:100), and anti-CD19 (1:200) antibodies
148 were applied on tissue sections along with one-hour incubation at room temperature in a
149 humidity chamber. The antigen-antibody bindings were detected with labeled polymer-HRP
150 Envision system (DAKO, K4007) and DAB+ chromogen (DAKO, K3468) system. Tissue sections
151 were briefly immersed in hematoxylin for counterstaining and were covered with cover glasses.
152
153 **Tissue digestion, Red blood cell lysis and Dead cell removal**
154
155 Ovarian cancer tissue obtained from the anatomic pathology department was transported in
156 DMEM/F12 containing 10% FBS and 1% P/S (10% DMEMF/12) on ice to the laboratory. Ovarian
157 cancer tissue was minced manually with a scalpel and enzymatically digested using 1.5 mg/ml
158 collagenase IV (Sigma-Aldrich), 1 mg/ml hyaluronidase (Sigma-Aldrich) and 500 μg/ml. DNase I
159 (GoldBio) in Hank's balanced salt solution (HBSS) in a 37 ^{0}C shaker (200rpm) for 0.5 – 2 h.
160 Following digestion, cells were resuspended in 10% DMEMF/12 and filtered serially through 70
161 μm and 40 μm strainers. Red blood cells were lysed by incubating the cell suspension in RBC lysis
162 buffer (Sigma-Aldrich) for 2-5 minutes. Lysis was quenched by adding excess 10% DMEMF/12.
163 The number of live cells was enriched using the dead cell removal kit (Miltenyi Biotec, 130-090-
164 101) according to manufacturer's instructions.
165
166 **Drop-seq Experiments**
167
168 Drop-seq experiment was performed as previously described[12]. Briefly, cells and barcoded beads
169 were loaded at a concentration of 100,000 cells/ml in PBS-BSA and 120,000 beads/ml in lysis
170 buffer in separate 3 ml syringes. Drop-seq experiments were run using a 125-micron microfluidic
171 device at 16 ml/hr (oil), 4 ml/hr (cells) and 4 ml/hr (beads) with ~15 minutes per collection.
172 Following collection, drops were broken and barcode beads with mRNA hybridized unto them
173 were collected and washed. Barcoded cDNA attached to the barcode beads or STAMPS were

174 generated by reverse transcription, treated with exonuclease 1 and the number of STAMPs was
175 counted. 5000 STAMPSs were aliquoted per well in a 96-well plate and the cDNA attached to the
176 STAMPS were amplified through 14 PCR cycles. PCR supernatants from each well were pooled
177 and cleaned with Ampure beads. Purified cDNA product was quantified using Qubit 3.0
178 (Invitrogen) and 450-650 pg of each sample was used as input for Illumina Nextera reactions (12
179 cycles). Tagmented libraries were quantified using an Agilent BioAnalyzer High sensitivity chip
180 according to manufacturer's recommendations before submission for sequencing on Illumina's
181 Nextseq 500, using NextSeq 75 cycle v3 kits. Paired end sequencing was performed on the
182 samples with 5% Illumina PhiX Control v3 added, with 20 bp for Read 1 and 64 bp for Read2 using
183 custom Read1 primer, GCCTGTCCGCGGAAGCAGTGGTATCAACGCAGAGTAC, according to
184 manufacturer's instructions.
185
186
187
188 From alignment of the reads collected from the Dropseq experiments, read count matrices for
189 unique molecular identifiers (UMIs) were generated for both exon regions and intronic regions
190 in the human genome (gencode hg38 v.27) using the STAR version 2.5.3 aligner[13,14]. The ovarian
191 cancer samples from patients' metastatic site omentum were sequenced with Drop-seq. A total
192 of 13 sequencing runs were performed for six patients metastatic site samples using Drop-seq
193 where each sample was sequenced twice to maximize the sequencing depth and 3401 sample
194 was sequenced three times. Each sequencing run produced paired-end reads, with one pair
195 representing the 12 bp cell barcode and six bp unique molecular identifier (UMI), and the second
196 pair representing a 60 bp mRNA fragment. The paired-end reads from the same samples were
197 merged and six paired-end fastq files were generated. A snakemake protocol based pipeline was
198 applied to process the paired-end reads from each sequencing run and produce a count matrix
199 representing the expression of every gene in every cell (Supplementary Methods)[15]. Individual
200 count matrices were produced for each of the six patients after accounting for UMI duplicates.
201
202 The individual count matrix was produced for each patient with a total number of six count
203 matrices. The summarized counts for each gene were inferred based on both exon and intronic
204 reads to produce the gene expression matrix per sample. Expression matrices of six ovarian
205 cancer samples from the metastatic sites in the omentum were generated. To select high quality
206 cells, we applied a filter based on the number of genes detected per cell. Prior to filtering, each
207 sample produced approximately 5000 cells. Based on the median number of genes captured, cells
208 with less than 800 genes were removed from the data sets. For lower quality samples, the
209 threshold was lowered to 600 to 700 as shown in Table 2. We followed a standardized pipeline
210 implemented in single cell analysis tool suite Seurat v3.0.2 [16,17]. A global-scaling normalization
211 method that normalizes the feature expression measurements for each cell by the total
212 expression, multiplies this by a scale factor of log (TP10k) was applied to all samples[17]. Each
213 normalization matrix was then scaled by a linear transformation to center the mean gene
214 expression of cells and normalized the gene expression variance. We applied PCA on the
215 normalized expression matrix to extract the variable components in the sample data, followed
216 by a heuristic elbow plot on the variance of each PC. We selected the number of top variant PCs
217 based on the elbow plot and the number varies from 10 to 15 depending on the sample. The top

PCs were used in further exploration of the data, such as UMAP /tSNE dimension reduction, construction of K-nearest neighbor graph and other graphical clustering analysis.

Cell type classification (correlation with CellAtlas)

To assign the cell type to individual cells, we used a bulk sequencing gene expression data-set from 95 cell lines collected by Cell Atlas[18] which cover 33 majority of cell types in normal human tissue, including common immune cells, endothelial, epithelial, fibroblast, mesodermal cells and so on. The cell lines can be further divided in to fine-grained 60 subtypes. We inferred the similarity between individual cells in the samples and cell lines by calculating the pairwise Pearson correlation matrix C={c(i,j)} among any cell, i, from the Drop-seq experiments with any cell line, j, in the cell atlas. We performed a shared nearest neighbor (SNN) modularity optimization-based clustering on the CellAtlas cell lines to group the cell lines into larger and more general cell type categories. This was done to eliminate the bias in CellAtlas dataset and remove some rare or under-powered cell types. The resulting clusters of cell lines were annotated by the most frequent major cell type from the cell line groups. For each cell in our cancer sample, the cell type was then assigned with the most common cell type from top 5 highly correlated major cell type clusters. We collapsed few ambiguous cell types with the neighboring cell types based on their expression profiles. The cell sub-type was assigned with the most highly correlated cell-type from the 60 sub-types in the cell lines.

Classification with cluster markers, canonical genes, and genetic functions

Sometimes the Gene Ontology (GO) and Pathway analysis gives general/noisy functional categories which make certain cell types hard to be identified. By leveraging prior knowledge from the CellAtlas mapping, we were able to locate the relevant function categories for those cell types and narrow down their marker genes more efficiently[18]. Moreover, by the consensus of both GO and CellAtlas analyses, we obtained higher confidence in classifying cell types in each patient sample.

We used the cell types obtained from the cell Atlas correlation as baseline and curated the cell types manually using canonical genes information and functional association for cell types detected. The differentially expressed gene markers were extracted from cell clusters. Cross-referencing was done between gene markers and known canonical genes to the cell types. Gene ontology and pathway-based enrichment was performed on the gene markers to provide additional evidence for the cell type assignment. As a result, we identified 9 major cell types which include epithelial cells, fibroblast cells, three immune cell types, viz., B cells/B cell plasma, T cells, and monocytes, mesenchymal stem cells (MSC), embryonic stem cells (ESC), and endothelial cells.

Trajectory analysis

We selected cells based on the classified cell types and performed trajectory analysis using monocle for single cell type and monocle 3 for multi-cell types[19,20]. The trajectory analysis in

262 monocle was to reduce the high dimensional gene expression matrix onto a tree structure using
263 DDR tree[20]. This method produces a single tree with multiple branches. The monocle3 was based
264 on UMAP dimension reduction and the resulting trajectory can be disconnected so that the
265 trajectory path for various cell types can be shown simultaneously[21].
266
267
268 # Results
269
270 **Patient cohort**
271
272 Ovarian cancer samples were collected from the metastatic site (the omentum) of six patients
273 (Table 1). Four patients were diagnosed with high grade serous cancer, one with serous
274 carcinoma and one with malignant mixed Mullerian tumor (MMMT). The ages of the patients
275 ranged from 46 to 71 years. All tumors were diagnosed at stage III or later. Four of the patients
276 had received neo-adjuvant therapy prior to surgery including the patient diagnosed with MMMT.
277 The reported ethnic background of patients includes two Whites, two Blacks and two Asians.
278
279 **Characteristics of the Tumor microenvironment**
280
281 Normal omentum is comprised mainly of adipocytes as well as aggregates of leukocytes called
282 milky spots[22]. Adipocytes act as a source of energy for ovarian cancer during invasion of the
283 omentum[10]. This results in an inverse relationship between ovarian tumor growth (cancer and
284 cancer associated cell growth) and reduction of adipocytes within the omentum[10]. The area of
285 tumor occupied by adipocyte decreases with disease score[23]. To quantify the transformation of
286 the omentum by ovarian cancer cells, we used Imagescope, a digital histopathology software, to
287 annotate and calculate the area occupied by adipocyte in each patient sample on hematoxylin
288 and eosin (H&E) stained sections (Figure 1A.) The area of adipocyte was reported as a percentage
289 of the total surface area of the sample used as a measure of disease score as previously described
290 by Pearce et al.[23] which we also used (Figure 1B). Two samples, PT-3401 and PT-5150 had the
291 highest percent area of adipocyte which we categorized as low disease score while the other 4
292 samples are categorized as high disease score. The presence of cancer cells, total stromal cells
293 and immune cells were confirmed by immunohistochemistry (IHC) using antibodies against
294 cytokeratin-7 (CK-7), vimentin and CD45 antibodies (Figure 1C-H). There was a varying proportion
295 of each cell type across patients. Notably, we observed that malignant cells in some patients (PT-
296 5150, PT- 3232, PT-4806 and PT-2834) double stained for CK-7 and vimentin suggesting active
297 epithelial mesenchymal transition (Figure 1C-F). In addition, the MMMT (PT-2834) sample had
298 two different types of malignant cells that stained separately for CK7 and vimentin. Incidentally,
299 the proportion of vimentin staining cells made up by $CD45^+$ immune cells positively correlated
300 with the area of adipocytes (Figure 1B&H). We also observed that these immune cells were
301 enriched around the remaining adipocytes and sparsely throughout the rest of the tissue.
302 Together, these data reveal patient variability in cancer cells in different histological types of
303 ovarian cancer and positively correlates the presence of adipocytes and immune cells.
304

305 **Generation of single cell Data, Cell-type clustering and cell type assignment**
306
307 For Drop-seq experiments, tumors samples were enzymatically digested into a single cell
308 suspension and ran through drop-seq experiment as previously described[12]. We integrated all six
309 omentum samples resulting in a gene expression matrix which contains the expression values of
310 9885 cells and 40947 genes mapped from the human reference genome (version GRCh38). A
311 minimum cut off of 600-800 genes per cell was set as shown in Table 2. The clustering was
312 performed by hierarchical clustering using resolution of 0.2 where 12 clusters are detected
313 (Figure 2A). The cells from each sample have membership across all clusters (Figure 2B). For each
314 cluster, a one-against-all upregulated markers detection was performed using Wilcoxon Rank
315 Sum test and genes with adjusted P-value < 0.05 were identified as significantly upregulated gene
316 markers. The dimension reduction was done using both t-SNE and UMAP and was found to be
317 consistent. The cell types were assigned and curated by cell line correlation, canonical genes and
318 functional categories for the significantly differentially express genes on the detected clusters. 9
319 major clusters out of 12 were identified with cell types (Figure 2C). This included 1 cluster for
320 malignant cells, 1 cluster for fibroblast, 1 cluster for mesenchymal stem cells, 1 cluster for
321 embryonic stem cells, 1 cluster for endothelial cells. Unsupervised clustering of the total cell
322 population of the different patients revealed three groups (Figure 2D); the first group (PT-6885
323 and PT-4806) had high ratios of epithelial and fibroblast clusters. The second group had a high
324 epithelial and T cell ratio (PT-3401 and PT-5150) and the final cluster was driven by a high
325 epithelial cell ratio (PT-3233 and PT-2834). Neo-adjuvant therapy has been previously described
326 to shift the cellular landscape from epithelial to immune cells in high grade serous ovarian cancer
327 samples[24]. Although we had 4 neo-adjuvant treated patient samples, only two (PT-6885 and PT-
328 4806) clustered together in the epithelial/fibroblast group. The neoadjuvant treated sample in
329 the epithelial group was from the MMMT patient with no significant shift to immune cells.
330 Finally, the neo-adjuvant sample in the high T cell group had the highest percentage of immune
331 cells. These scRNA-seq data reconfirms the heterogeneous nature of the tumor environment as
332 well as the heterogenous response to therapy.
333
334 **Cancer cell clustering analysis**
335
336 All 6 patient samples were merged and cells belonging to the central clusters connected to
337 epithelial cells shown in Figure 3 were selected. The corresponding cell types are epithelial cells
338 and ESC according to the cell types assignment results from all cellsAtlas[18]. There was a total of
339 4,733 cells in this subset. We detected 7 clusters using resolution 0.2 (Figure 3A&B). Cluster 0
340 and 3 highly expressed EpCAM (Figure 3E) that has previously been associated with platinum
341 resistance and metastasis in ovarian cancer[25]. Cluster 0 expressed the highest levels of IL-6 and
342 TGF-β (Figure 3C&D). IL-6 enhances tumor cell survival and platinum resistance and correlates
343 with poor prognosis in ovarian cancer while TGF-β induces an aggressive cancer phenotype [26-29].
344 In addition to EpCAM, Cluster 3 highly expressed NDRG1 and other epithelial markers such as
345 KRT18, KRT19 and CD24 (Figure 3E). NDRG1 is activated by p53 and was shown to inhibit
346 proliferation of metastatic lung cancer cells [30,31]. Another ovarian cancer marker, PAX8, was
347 expressed by cluster 2, along with high expression of MALAT1 and MUC16 (Figure 3E). High
348 expression of MALAT1 is associated with advanced disease, recurrence and reduced survival[32].

349 MUC16 is a biomarker of ovarian cancer and necessary for tumor cell growth and metastasis[33,34].
350 Cluster 1 expressed vimentin along with high MKI67 and PCLAF indicative of a proliferating
351 population. Cluster 5 also expressed PCLAF, a marker of proliferation, as well as FN1 and ZEB1
352 that are markers of epithelial to mesenchymal transition (EMT). Cluster 6 highly expressed
353 vimentin, MKI67 (marker of proliferation), S100A4, a protein implicated in tumor and progression
354 and metastasis(Figure 3E)[35]. These highly expressed markers, along with comparatively lower
355 expression of EMT markers (ZEB1 and ZEB2) in cluster 6 are suggestive of cells undergoing
356 mesenchymal to epithelial transition (Figure 3E). We also investigated the presence of clusters
357 expressing classical ovarian cancer stem cells markers including CD33, CD44, CD117 and CD24[36].
358 However, we did not observe cells co-expressing these markers, which may be due to the
359 problem of low sensitivity and drop-outs in our single-cell data. These distinctive clusters reveal
360 the heterogeneity within ovarian cancer population at any given time and the multiple processes
361 that cancer cells harness to progress disease.
362
363 **Immune cellular profile of patient samples**
364
365 The milky spots of the omentum is normally composed of 70% macrophages, 10% T cells and 10%
366 B cells along with mast cells and stromal cells[22]. During the initial phase of metastasis and
367 colonization of the omentum, additional macrophages are recruited from the peritoneal cavity
368 without any anti-tumor effect on the cancer cells[37,38]. The presence of T cells positively correlates
369 with overall survival[39,40]. To further investigate the immune population in the metastatic
370 omentum tissue, we selected the immune cells from the six patient samples and divided the cells
371 into 3 major categories T cell (956), B cell (409)/B cell plasma (358) and monocytes (695). The T
372 cells can be further divided into CD4 and CD8 positive clusters based on the violin plot of the CD4
373 and CD8 genes. B cells and plasma cells were distinguished by the B cell specific marker gene
374 CD19 where the expression of CD19 was turned down in plasma cells. The monocytes exhibited
375 a combination of macrophages and monocytes. Similar samples were grouped by a dendrogram
376 resulting in 2 main groups (Figure 4A): 1) a T cell signature group (2 samples) and 2) a monocyte
377 signature group (4 samples). These groups are similar to our previously described low and high
378 disease score (Figure 1). In addition, the high T cell group also expressed a high B cell signature
379 which was absent in the samples with the monocyte/macrophage signature group. Interestingly,
380 there was a difference in the samples of the high T cell group between the neo-adjuvant (PT-
381 5150) and the non-neoadjuvant treated sample (PT-3401). The neoadjuvant sample had a higher
382 ratio of plasma B cells (64.4%) than the sample from the non-neo-adjuvant sample (28.0%)
383 (Figure 4B). Conversely the neoadjuvant sample had a lower ratio of B cell cluster
384 1(naïve/memory B cells) (35.6%) compared to the non-neo-adjuvant sample (72.0%). $CD20^+$ B
385 cells colocalized with $CD8^+$ T cells positively correlated with overall survival[41]. Contrastingly,
386 plasma cell infiltration in epithelial ovarian cancer significantly reduced overall survival[42]. Taken
387 together this data suggests there is varied immune response to neoadjuvant therapy amongst
388 sample/patients and a need for personalized novel therapies.
389
390 **Differences in T cell clustering and subtype analysis**
391

392 We classified the 6 omentum samples into two disease groups based on the adipocyte ratio
393 detected in the samples as well as the dendrogram grouping. Higher disease score (HighDS)
394 corresponds to lower adipocyte and T cell ratio while the low disease score (LowDS) group had
395 higher adipocyte and T cell ratio. The HighDS group (samples PT- 4806, PT-6885, PT-2834, PT-
396 3233) and LowDS group yielded 5190 and 4695 total cells respectively. To reveal the functional
397 subtypes of T cells and any difference in the HighDS versus LowDS groups, we clustered a total of
398 956 total T cell, 820 LowDS T cells and 136 HighDS T cells (Figure 5A). A total of 4, 4 and 3
399 transcriptionally distinct clusters emerged from total, LowDS and HighDS T cells respectively.
400 (Figure 5A-C). The top genes revealed clusters similar to previously described T cell phenotypes
401 in breast cancer including $CD4^+$IL7R, $CD4^+$FOXP3, resident memory$CD8^+$T cells ($CD8^+$Trm cells) and
402 one population described in lung cancer with high granulysin expression $CD4^+$GNLY[43,44]. Although
403 there were fewer T cells in the HighDS group they clustered into 3 groups. Both groups had
404 LowDS group. $CD8^+$Trm cells had the highest expression of IFN-γ in both groups (Figure 5B).
405 Additionally, although both groups had $CD8^+$Trm cells, only the $CD8^+$Trm cells (P value < 0.004) in
406 the LowDS group expressed a recently described transcription factor, TOX, which is the master
407 regulator of exhausted T cells (Figure 5C)[45,46]. TOX was also lowly expressed by the $GNLY^+$T cells
408 (p value = 0.407). These TOX^+ T cells persist during chronic infection and TOX is expressed on the
409 $CD8^+$T cells that are reactivated in response to PD-L1 immunotherapy. These data suggest that
410 scRNA-seq is capable of determining patients that will benefit from novel therapy.
411
412 **Transcriptionally distinct plasma cell clusters in LowDS group.**
413
414 B cells studies in ovarian cancer has been limited to their effect on survival. $CD20^+$ B cells
415 colocalized with $CD8^+$ T cells positively correlated with overall survival[41]. Contrastingly, plasma
416 cell infiltration in epithelial ovarian cancer significantly reduced overall survival[42]. These surface
417 markers alone are not informative about the transcriptional state or function of B cells. To
418 investigate the B cell subtypes in our samples, B cells and plasma cells were distinguished by the
419 B cell specific marker gene CD19 where the expression of CD19 was turned down in plasma cells.
420 In the LowDS group there were a total of 396 B cells and 274 plasma cells while there was a total
421 of 124 B cells detected in the HighDS group. Unsupervised clustering on combined B cells
422 revealed a total of 3 clusters (Figure 6A); naïve/effector B cells, plasma B cells and a third cluster
423 enriched with cycling genes. When we performed unsupervised clustering on the two groups
424 separately, the LowDS and HighDS group had 4 and 2 clusters respectively (Figure 6B&C). In the
425 LowDS group, cluster 0 had high expression of MHC class II genes, cluster 1 and 2 were both
426 positive for BLIMP1 indicating they are plasma cells. However, cluster 2 highly express CD38 and
427 CD138 indicative of post germinal center B cells. Both cluster 1 and 2, highly expressed class
428 switched IGHG. Finally, cluster 3, highly expressed proliferative genes and low Blimp1 suggesting
429 a plasmablast population. In the HighDS group, cluster 0 highly expressed CD24 a naïve B cell
430 marker while cluster 1 highly expressed BLIMP1. Post germinal center B cells were absent in this
431 group.
432
433 **Identification of novel macrophage subsets**
434

The samples assigned to the HighDS group had a low T cell to monocyte ratio (0.4: 1) compared to the LowDS group (2.5:1). To assess the differences in the macrophage population, we performed unsupervised clustering on both groups combined (Figure 7A) and separately (Figure 7B&C). There were 4 clusters in the LowDS group and 2 clusters in the highDS. Both groups had a $CD14^{+}CD16^{+}CD163^{+}$ cluster reminiscent of tumor associated macrophages. In the highDS group, there was also an immature $CCR7^{+}FLT3^{+}$ population. These $FLT3^{+}$ progenitors can differentiate into osteoclasts, dendritic cells, microglia and macrophages[47]. The other clusters in the high T cell group included $CCR7^{+}CD274^{+}$ which suggest a regulatory population likely similar to MDSCs. $IRF8^{+}$ expressing macrophages (Cluster 2) are induced in the presence of IFN-γ and promote the formation of autophagosome[48]. The final cluster highly expressed NR1H2 inhibits inflammatory genes in macrophages[49,50].

Discussion

In this study we analyzed approximately 10,000 cells from 6 patients with 3 histotypes of epithelial ovarian cancer at the most common metastatic site, the omentum. The resolution of our dataset revealed 9 major clusters of which we further interrogated the cancer and immune cells clusters. The concurrent transcriptomic analysis of cancer and stromal cells provides insights into the interactions occurring within the tumor microenvironment that contribute to the progression of cancer. Our single cell data was able to stratify our patients into two groups based on their immune response.

The largest cluster of cells was cancer epithelial cells, which composed about 50% of cells analyzed. These cells expressed a variety of genes associated with metastatic disease including MUC16, PAX8 and MALAT1. Although we combined cells from 6 different patients, cancer cells from each patient expressed a variety of these markers indicating that targeting any of these genes will be redundant since there are compensatory proteins that will continue to progress disease. Another approach to targeting tumors will be the identification of cancer stem cell in ovarian cancer[51]. Many studies have attempted to identify these rare cells without success[52,53]. We did find a cell population closely resembling embryonic stem cells that highly express proliferative markers. Successful identification for isolation and interrogation of these putative ESC cells might provide useful insight about CSC cells in ovarian cancer.

Infiltration of immune cells into the omentum during metastatic cancer does not always elicit anti-tumor responses[38]. In ovarian cancer, high tumor infiltrating T cells is associated with significantly longer overall survival[11]. However not all patients have a high infiltration of T cells. Additionally, the transformation of adipocytes into cancer cell described here inversely correlates with the number of infiltrating immune cells. The mechanisms behind this difference in immune response remains incompletely understood. There is evidence that associates immunogenicity of neo-antigens generated due to high tumor mutational load and clinical response to immunotherapies[54-57]. The functional plasticity of leukocytes makes them an attractive therapeutic target. Additionally, immunotherapy avoids the obstacle of drug delivery in solid

tumors by using the cells within the tumor environment to target therapy, making cancer immunotherapy an area of high investigation. To this end, we sought to investigate the immune population within these metastatic tumors. From the 6 patients we investigated in this study, 2 of them had a high T cell response while the other 4 had a high monocyte response. Once we grouped our data into two different immune groups we sought to reconcile the transcriptomic signature in the cancer cells with the immune response. Both high T cell and high monocyte groups had 8 cancer cell cluster. Was there any difference in these cells?

Advances in personalized medicine has revealed TOX as a transcription factor expressed by T cells that respond to immune checkpoint block[45,58]. In our patient cohort, TOX was expressed by two T cell subsets, $CD8^+$Trm and $CD4^+$GNLY in the high T cell group. The high monocyte group also had the $CD8^+$Trm subset but not the $CD4^+$GNLY subset. Interestingly, there was no TOX expression in the high monocyte group. TOX confers longevity and persistence on T cell in immunosuppressive environment such as cancer; however, the mechanism by which these TOX^+ T cells are generated is not understood. Coincidentally, there is also a difference in the B cell population. Along with the expression of TOX in T cells, the high T cell response group also had a unique subset of $BLIMP1^+CD38^+CD138^+$ B cell population. It is likely that these antigen cognate plasma B cells are involved in the generation or maintenance of TOX^+ T cells. A mechanistic study of these cells is necessary as they may hold the key into inducing TOX^+T cells in patients who do not respond to immune checkpoint inhibitors.

Conclusion

To our knowledge, this is the first scRNA-seq study that allows stratification of patients according to immune response in metastatic ovarian cancer. Concurrent transcriptomic analysis of cancer and stromal cells revealed intratumor heterogeneity and patient variability highlighting the need for personalized medicine. Interrogating tumor infiltrating lymphocytes at the single cell level also feature unique differences in other tumor infiltrating immune cells that are previously undescribed. Mechanistic studies are required to determine the role of these cells in tumor progression and response to novel cancer immunotherapies.

Acknowledgement

We are grateful to Mengjie Chen for helpful discussions on CellAtlas data and Mark Lingen for help with tissue access. This work was performed, in part, at the Center for Nanoscale Materials, a U.S. Department of Energy Office of Science User Facility, and supported by the U.S. Department of Energy, Office of Science, under Contract No. DE-AC02-06CH11357. All patient tissues were histologically graded, de-identified and obtained from the University of Chicago Human Tissue Resource Center. Computational resources and data storage were provided by the University of Chicago Research Computing Center.

521

522 # References

523

524 1 Siegel, R. L., Miller, K. D. & Jemal, A. Cancer Statistics, 2017. *CA: a cancer journal for*
525 *clinicians* **67**, 7-30, doi:10.3322/caac.21387 (2017).
526 2 Testa, U., Castelli, G. & Pelosi, E. Genetic Abnormalities, Clonal Evolution, and Cancer
527 Stem Cells of Brain Tumors. *Med Sci (Basel)* **6**, doi:10.3390/medsci6040085 (2018).
528 3 Zheng, G. X. *et al.* Massively parallel digital transcriptional profiling of single cells. *Nat*
529 *Commun* **8**, 14049, doi:10.1038/ncomms14049 (2017).
530 4 Villani, A. C. *et al.* Single-cell RNA-seq reveals new types of human blood dendritic cells,
531 monocytes, and progenitors. *Science* **356**, doi:10.1126/science.aah4573 (2017).
532 5 Dixit, A. *et al.* Perturb-Seq: Dissecting Molecular Circuits with Scalable Single-Cell RNA
533 Profiling of Pooled Genetic Screens. *Cell* **167**, 1853-1866 e1817,
534 doi:10.1016/j.cell.2016.11.038 (2016).
535 6 Jaitin, D. A. *et al.* Dissecting Immune Circuits by Linking CRISPR-Pooled Screens with
536 Single-Cell RNA-Seq. *Cell* **167**, 1883-1896 e1815, doi:10.1016/j.cell.2016.11.039 (2016).
537 7 Shalek, A. K. *et al.* Single-cell transcriptomics reveals bimodality in expression and splicing
538 in immune cells. *Nature* **498**, 236-240, doi:10.1038/nature12172 (2013).
539 8 Zheng, C. *et al.* Landscape of Infiltrating T Cells in Liver Cancer Revealed by Single-Cell
540 Sequencing. *Cell* **169**, 1342-1356 e1316, doi:10.1016/j.cell.2017.05.035 (2017).
541 9 Clark, R. *et al.* Milky spots promote ovarian cancer metastatic colonization of peritoneal
542 adipose in experimental models. *The American journal of pathology* **183**, 576-591,
543 doi:10.1016/j.ajpath.2013.04.023 (2013).
544 10 Nieman, K. M. *et al.* Adipocytes promote ovarian cancer metastasis and provide energy
545 for rapid tumor growth. *Nature medicine* **17**, 1498-1503, doi:10.1038/nm.2492 (2011).
546 11 Santoiemma, P. P. & Powell, D. J., Jr. Tumor infiltrating lymphocytes in ovarian cancer.
547 *Cancer Biol Ther* **16**, 807-820, doi:10.1080/15384047.2015.1040960 (2015).
548 12 Macosko, E. Z. *et al.* Highly Parallel Genome-wide Expression Profiling of Individual Cells
549 Using Nanoliter Droplets. *Cell* **161**, 1202-1214, doi:10.1016/j.cell.2015.05.002 (2015).
550 13 Frankish, A. *et al.* GENCODE reference annotation for the human and mouse genomes.
551 *Nucleic Acids Res* **47**, D766-D773, doi:10.1093/nar/gky955 (2019).
552 14 Dobin, A. *et al.* STAR: ultrafast universal RNA-seq aligner. *Bioinformatics* **29**, 15-21,
553 doi:10.1093/bioinformatics/bts635 (2013).
554 15 Selewa, A. *et al.* Systematic Comparison of High-throughput Single-Cell and Single-
555 Nucleus Transcriptomes during Cardiomyocyte Differentiation. *BioRxiv*,
556 doi:10.1101/585901 (2019).
557 16 Butler, A., Hoffman, P., Smibert, P., Papalexi, E. & Satija, R. Integrating single-cell
558 transcriptomic data across different conditions, technologies, and species. *Nature*
559 *biotechnology* **36**, 411-420, doi:10.1038/nbt.4096 (2018).
560 17 Stuart, T. *et al.* Comprehensive Integration of Single-Cell Data. *Cell* **177**, 1888-1902 e1821,
561 doi:10.1016/j.cell.2019.05.031 (2019).

562 18 Mabbott, N. A., Baillie, J. K., Brown, H., Freeman, T. C. & Hume, D. A. An expression atlas
563 of human primary cells: inference of gene function from coexpression networks. *BMC*
564 *Genomics* **14**, 632, doi:10.1186/1471-2164-14-632 (2013).
565 19 Trapnell, C. *et al.* The dynamics and regulators of cell fate decisions are revealed by
566 pseudotemporal ordering of single cells. *Nature biotechnology* **32**, 381-386,
567 doi:10.1038/nbt.2859 (2014).
568 20 Qiu, X. *et al.* Reversed graph embedding resolves complex single-cell trajectories. *Nat*
569 *Methods* **14**, 979-982, doi:10.1038/nmeth.4402 (2017).
570 21 Becht, E. *et al.* Dimensionality reduction for visualizing single-cell data using UMAP.
571 *Nature biotechnology*, doi:10.1038/nbt.4314 (2018).
572 22 Platell, C., Cooper, D., Papadimitriou, J. M. & Hall, J. C. The omentum. *World J*
573 *Gastroenterol* **6**, 169-176, doi:10.3748/wjg.v6.i2.169 (2000).
574 23 Pearce, O. M. T. *et al.* Deconstruction of a Metastatic Tumor Microenvironment Reveals
575 a Common Matrix Response in Human Cancers. *Cancer Discov* **8**, 304-319,
576 doi:10.1158/2159-8290.CD-17-0284 (2018).
577 24 Shih, A. J. *et al.* Correction: Identification of grade and origin specific cell populations in
578 serous epithelial ovarian cancer by single cell RNA-seq. *PloS one* **13**, e0208778,
579 doi:10.1371/journal.pone.0208778 (2018).
580 25 Bellone, S. *et al.* Overexpression of epithelial cell adhesion molecule in primary,
581 metastatic, and recurrent/chemotherapy-resistant epithelial ovarian cancer: implications
582 for epithelial cell adhesion molecule-specific immunotherapy. *Int J Gynecol Cancer* **19**,
583 860-866, doi:10.1111/IGC.0b013e3181a8331f (2009).
584 26 Coward, J. *et al.* Interleukin-6 as a therapeutic target in human ovarian cancer. *Clinical*
585 *cancer research : an official journal of the American Association for Cancer Research* **17**,
586 6083-6096, doi:10.1158/1078-0432.CCR-11-0945 (2011).
587 27 Lutgendorf, S. K. *et al.* Interleukin-6, cortisol, and depressive symptoms in ovarian cancer
588 patients. *Journal of clinical oncology : official journal of the American Society of Clinical*
589 *Oncology* **26**, 4820-4827, doi:10.1200/JCO.2007.14.1978 (2008).
590 28 Scambia, G. *et al.* Prognostic significance of interleukin 6 serum levels in patients with
591 ovarian cancer. *Br J Cancer* **71**, 354-356, doi:10.1038/bjc.1995.71 (1995).
592 29 Li, W. *et al.* TGFbeta1 in fibroblasts-derived exosomes promotes epithelial-mesenchymal
593 transition of ovarian cancer cells. *Oncotarget* **8**, 96035-96047,
594 doi:10.18632/oncotarget.21635 (2017).
595 30 Stein, S. *et al.* NDRG1 is necessary for p53-dependent apoptosis. *J Biol Chem* **279**, 48930-
596 48940, doi:10.1074/jbc.M400386200 (2004).
597 31 Ellen, T. P., Ke, Q., Zhang, P. & Costa, M. NDRG1, a growth and cancer related gene:
598 regulation of gene expression and function in normal and disease states. *Carcinogenesis*
599 **29**, 2-8, doi:10.1093/carcin/bgm200 (2008).
600 32 Gordon, M. A., Babbs, B., Cochrane, D. R., Bitler, B. G. & Richer, J. K. The long non-coding
601 RNA MALAT1 promotes ovarian cancer progression by regulating RBFOX2-mediated
602 alternative splicing. *Mol Carcinog* **58**, 196-205, doi:10.1002/mc.22919 (2019).
603 33 Robertson, D. M. *et al.* Combined inhibin and CA125 assays in the detection of ovarian
604 cancer. *Clin Chem* **45**, 651-658 (1999).

605 34 Theriault, C. *et al.* MUC16 (CA125) regulates epithelial ovarian cancer cell growth,
606 tumorigenesis and metastasis. *Gynecologic oncology* **121**, 434-443,
607 doi:10.1016/j.ygyno.2011.02.020 (2011).
608 35 Fei, F., Qu, J., Zhang, M., Li, Y. & Zhang, S. S100A4 in cancer progression and metastasis:
609 A systematic review. *Oncotarget* **8**, 73219-73239, doi:10.18632/oncotarget.18016 (2017).
610 36 Klemba, A. *et al.* Surface markers of cancer stem-like cells of ovarian cancer and their
611 clinical relevance. *Contemp Oncol (Pozn)* **22**, 48-55, doi:10.5114/wo.2018.73885 (2018).
612 37 Shimotsuma, M., Simpson-Morgan, M. W., Takahashi, T. & Hagiwara, A. Activation of
613 omental milky spots and milky spot macrophages by intraperitoneal administration of a
614 streptococcal preparation, OK-432. *Cancer research* **52**, 5400-5402 (1992).
615 38 Oosterling, S. J. *et al.* Insufficient ability of omental milky spots to prevent peritoneal
616 tumor outgrowth supports omentectomy in minimal residual disease. *Cancer Immunol*
617 *Immunother* **55**, 1043-1051, doi:10.1007/s00262-005-0101-y (2006).
618 39 Sato, E. *et al.* Intraepithelial CD8+ tumor-infiltrating lymphocytes and a high
619 CD8+/regulatory T cell ratio are associated with favorable prognosis in ovarian cancer.
620 *Proceedings of the National Academy of Sciences of the United States of America* **102**,
621 18538-18543, doi:10.1073/pnas.0509182102 (2005).
622 40 Wouters, M. C. *et al.* Treatment Regimen, Surgical Outcome, and T-cell Differentiation
623 Influence Prognostic Benefit of Tumor-Infiltrating Lymphocytes in High-Grade Serous
624 Ovarian Cancer. *Clinical cancer research : an official journal of the American Association*
625 *for Cancer Research* **22**, 714-724, doi:10.1158/1078-0432.CCR-15-1617 (2016).
626 41 Santoiemma, P. P. *et al.* Systematic evaluation of multiple immune markers reveals
627 prognostic factors in ovarian cancer. *Gynecologic oncology* **143**, 120-127,
628 doi:10.1016/j.ygyno.2016.07.105 (2016).
629 42 Lundgren, S., Berntsson, J., Nodin, B., Micke, P. & Jirstrom, K. Prognostic impact of
630 tumour-associated B cells and plasma cells in epithelial ovarian cancer. *J Ovarian Res* **9**,
631 21, doi:10.1186/s13048-016-0232-0 (2016).
632 43 Savas, P. *et al.* Publisher Correction: Single-cell profiling of breast cancer T cells reveals a
633 tissue-resident memory subset associated with improved prognosis. *Nature medicine* **24**,
634 1941, doi:10.1038/s41591-018-0176-6 (2018).
635 44 Guo, X. *et al.* Publisher Correction: Global characterization of T cells in non-small-cell lung
636 cancer by single-cell sequencing. *Nature medicine* **24**, 1628, doi:10.1038/s41591-018-
637 0167-7 (2018).
638 45 Yao, C. *et al.* Single-cell RNA-seq reveals TOX as a key regulator of CD8(+) T cell persistence
639 in chronic infection. *Nat Immunol* **20**, 890-901, doi:10.1038/s41590-019-0403-4 (2019).
640 46 Khan, O. *et al.* TOX transcriptionally and epigenetically programs CD8(+) T cell exhaustion.
641 *Nature* **571**, 211-218, doi:10.1038/s41586-019-1325-x (2019).
642 47 Servet-Delprat, C. *et al.* Flt3+ macrophage precursors commit sequentially to osteoclasts,
643 dendritic cells and microglia. *BMC Immunol* **3**, 15, doi:10.1186/1471-2172-3-15 (2002).
644 48 Gupta, M. *et al.* IRF8 directs stress-induced autophagy in macrophages and promotes
645 clearance of Listeria monocytogenes. *Nat Commun* **6**, 6379, doi:10.1038/ncomms7379
646 (2015).

49 Castrillo, A., Joseph, S. B., Marathe, C., Mangelsdorf, D. J. & Tontonoz, P. Liver X receptor-dependent repression of matrix metalloproteinase-9 expression in macrophages. *J Biol Chem* **278**, 10443-10449, doi:10.1074/jbc.M213071200 (2003).

50 N, A. G. & Castrillo, A. Liver X receptors as regulators of macrophage inflammatory and metabolic pathways. *Biochim Biophys Acta* **1812**, 982-994, doi:10.1016/j.bbadis.2010.12.015 (2011).

51 Bast, R. C., Jr., Hennessy, B. & Mills, G. B. The biology of ovarian cancer: new opportunities for translation. *Nat Rev Cancer* **9**, 415-428, doi:10.1038/nrc2644 (2009).

52 Shah, M. M. & Landen, C. N. Ovarian cancer stem cells: are they real and why are they important? *Gynecologic oncology* **132**, 483-489, doi:10.1016/j.ygyno.2013.12.001 (2014).

53 Burgos-Ojeda, D., Rueda, B. R. & Buckanovich, R. J. Ovarian cancer stem cell markers: prognostic and therapeutic implications. *Cancer letters* **322**, 1-7, doi:10.1016/j.canlet.2012.02.002 (2012).

54 Van Allen, E. M. *et al.* Genomic correlates of response to CTLA-4 blockade in metastatic melanoma. *Science* **350**, 207-211, doi:10.1126/science.aad0095 (2015).

55 Rizvi, N. A. *et al.* Cancer immunology. Mutational landscape determines sensitivity to PD-1 blockade in non-small cell lung cancer. *Science* **348**, 124-128, doi:10.1126/science.aaa1348 (2015).

56 Snyder, A. *et al.* Genetic basis for clinical response to CTLA-4 blockade in melanoma. *N Engl J Med* **371**, 2189-2199, doi:10.1056/NEJMoa1406498 (2014).

57 Aguade-Gorgorio, G. & Sole, R. Genetic instability as a driver for immune surveillance. *J Immunother Cancer* **7**, 345, doi:10.1186/s40425-019-0795-6 (2019).

58 Siddiqui, I. *et al.* Intratumoral Tcf1(+)PD-1(+)CD8(+) T Cells with Stem-like Properties Promote Tumor Control in Response to Vaccination and Checkpoint Blockade Immunotherapy. *Immunity* **50**, 195-211 e110, doi:10.1016/j.immuni.2018.12.021 (2019).

691
692
693
694
695
696
697
698

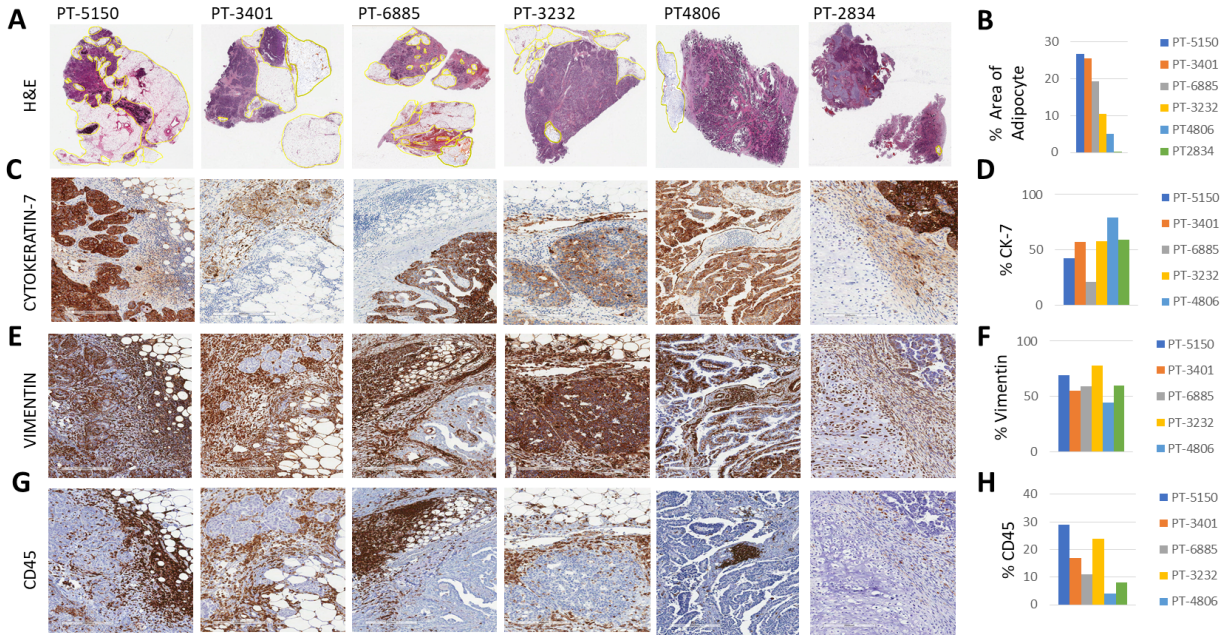

Figure 1: A) The hematoxylin and eosin (H&E) stained sections with B) the percentage area of adipocytes histogram on the individual patient sample. C) Cytokeratin-7 (CK-7) staining on patient sample slices with D) the percentage of CK-7 positive histogram on the individual patient sample. E) Vimentin staining on patient sample slices with F) the percentage of Vimentin positive histogram on the individual patient sample. G) CD45 staining on patient sample slices with H) the percentage of CD45 positive histogram on the individual patient sample. Images taken at A) 40x ; C),E),G) 160x

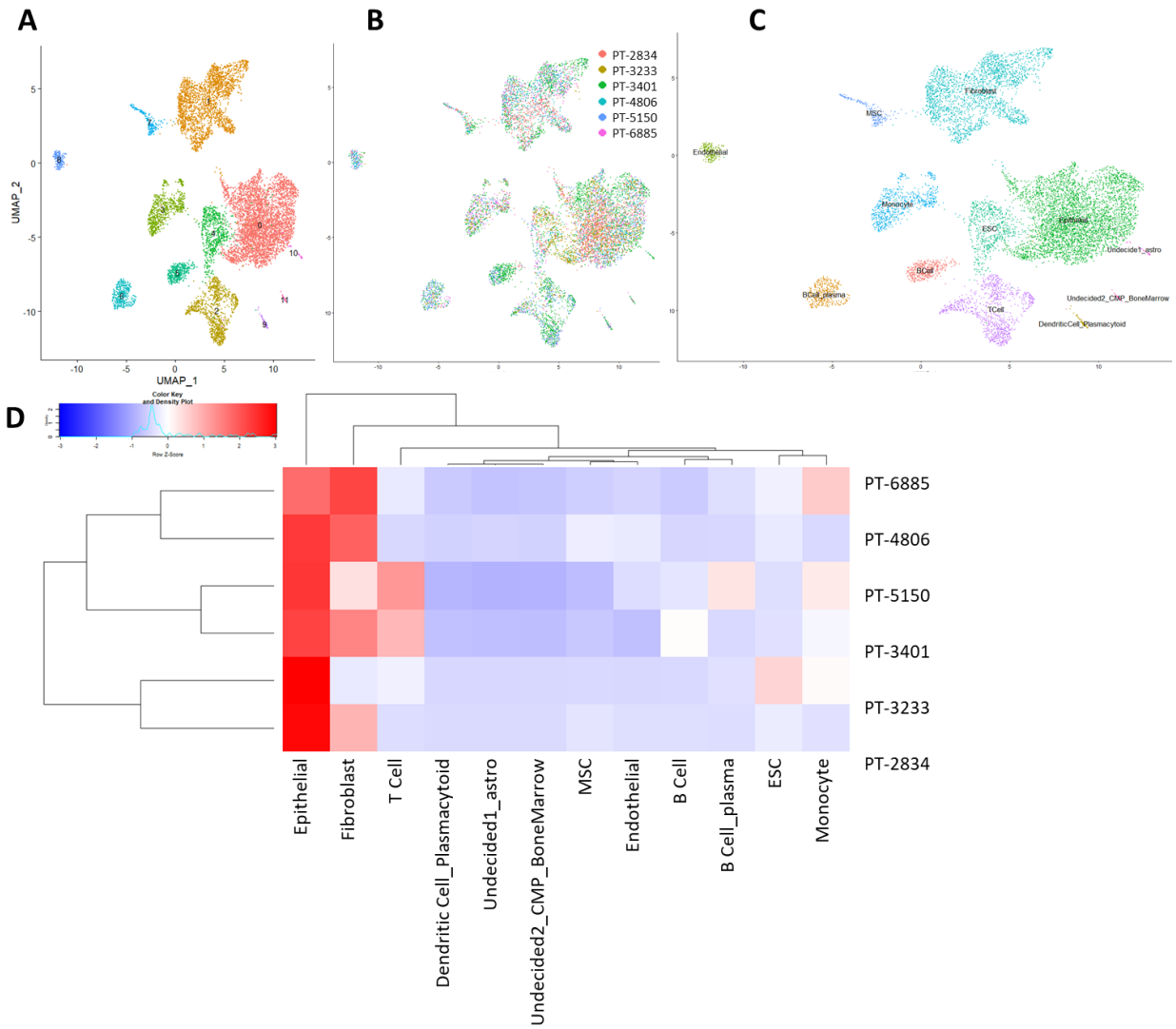

Figure 2: A) UMAP plot for high-quality cells, based on number of genes detected per cell in all six omentum samples, colored by clustering results. B) The UMAP colored by the patients. C) UMAP plot for clusters colored and annotated by assigned cell types. D) Heatmap of cell types composition ratio in each patient sample with hierarchical dendrograms on both patients and cell types.

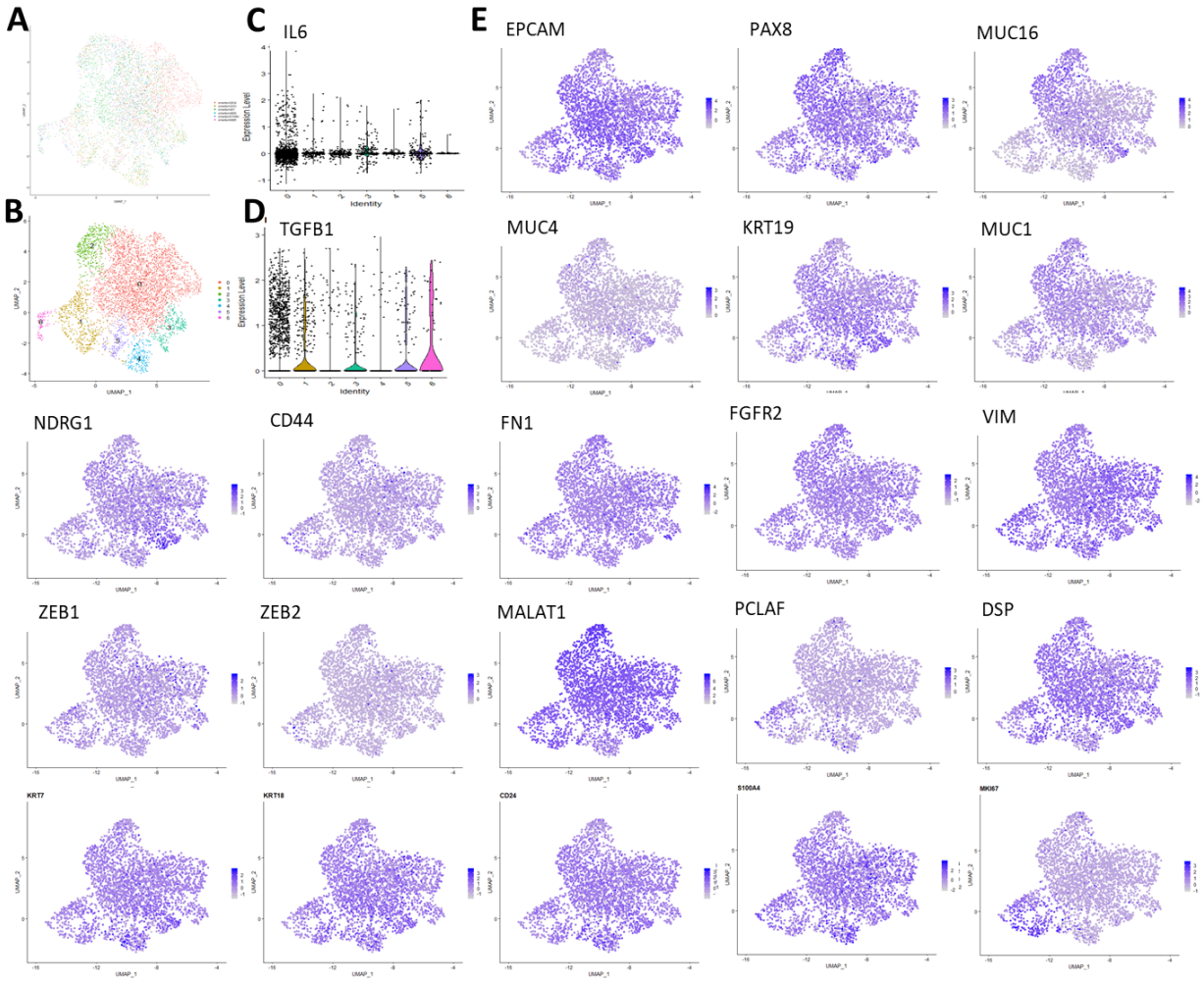

Figure 3: A) UMAP plot for annotated cancer cell-types only from all six omentum samples and colored by patient. B) UMAP plot colored by unsupervised clustering results. C) Violin plot for gene IL-6 expression level across all seven clusters. D) Violin plot for gene TGFB1 counts across all seven clusters. E) Feature plots of relevant marker genes.

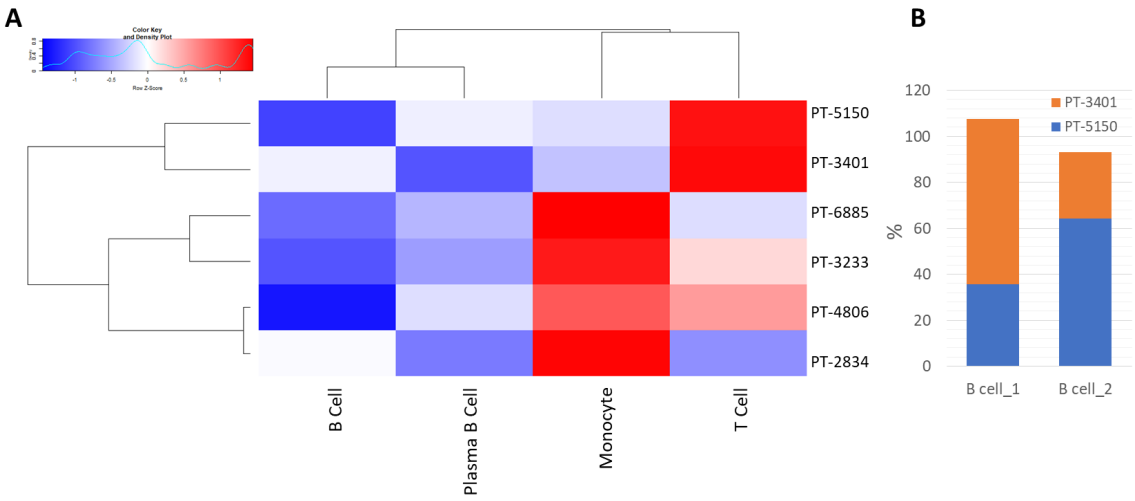

Figure 4: A) Heatmap of immune cell types (T cell, B cell, plasma B cell, and Monocyte in each patient sample with vertical and horizontal dendrograms on both patients and cell types. B) The overall percentage of two B cell populations (B cell 1: naïve B cell; B cell 2: plasma B cell) in low disease score group, PT-3401 and PT-5150.

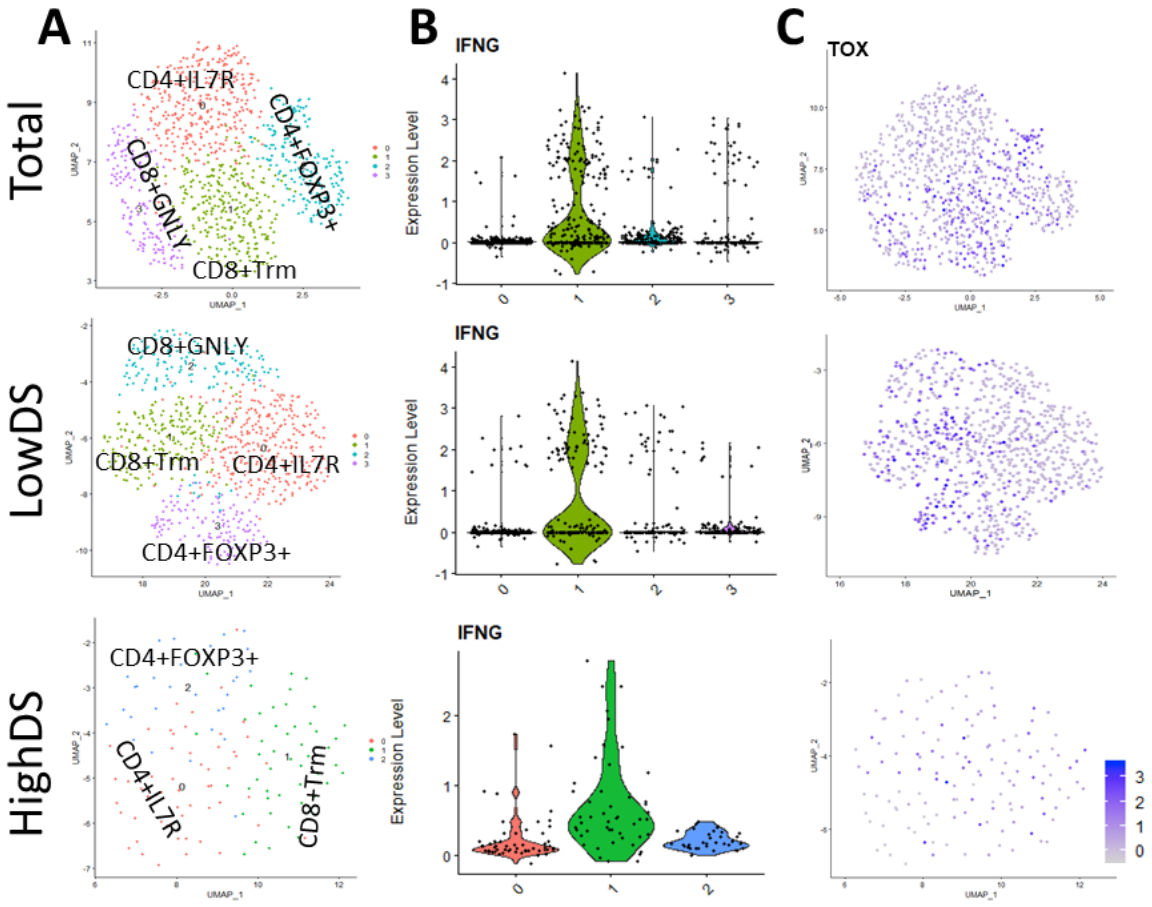

Figure 5: A) UMAP plot for T cells in across all six samples, annotated by T cell sub-population for total, low and high disease score. B) The violin plot of gene IFNG expression level across four T cell sub-populations in all six samples. C) The feature plot for expression level of gene TOX in low disease score samples.

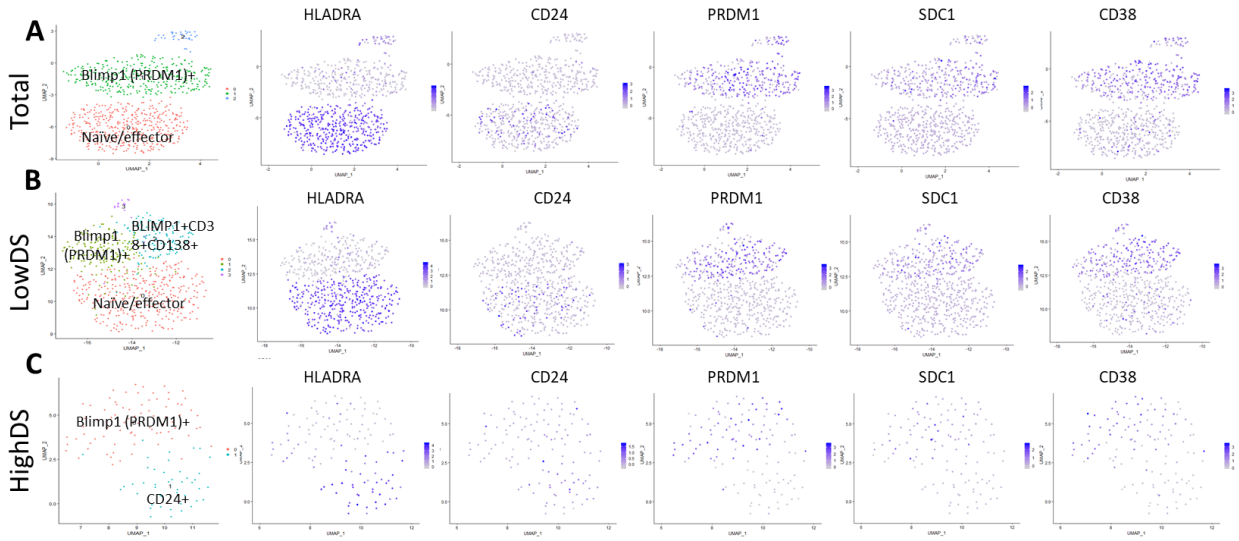

Figure 6. UMAP plot for B cells in all six samples, annotated by B cell sub-population A) total B) low disease score group C) high disease score group along with feature plots for marker genes.

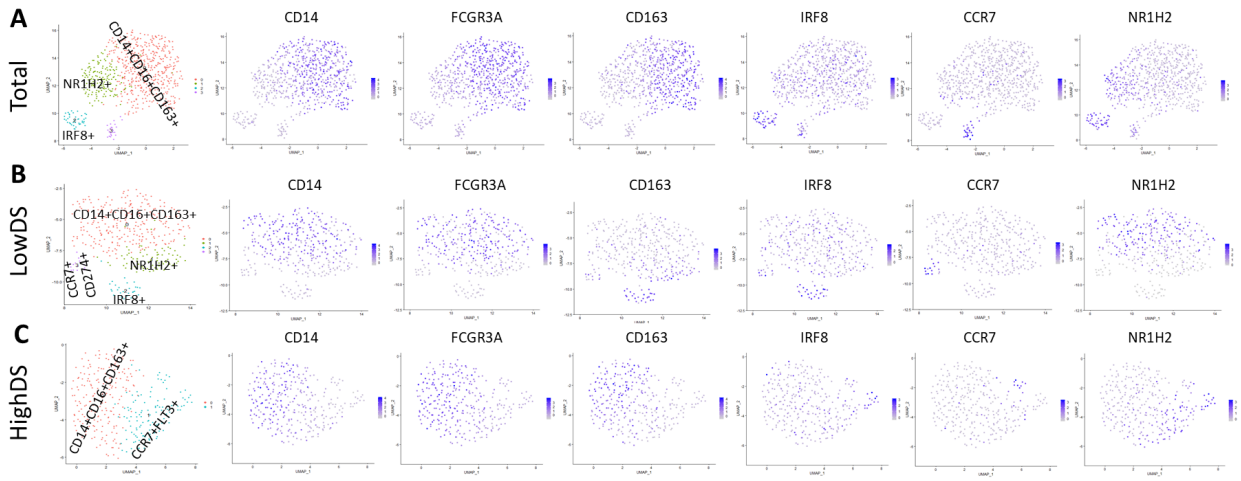

Figure 7. UMAP plot for monocytes in all six samples, annotated by monocyte sub-population in A) total B) low disease score group C) high disease score group along with feature plots for marker genes.

Omentum	Age	Race	Origin	Histologic type	Histological grade	Neoadjuvant therapy	Stage (PMN/FIGO)
PT-3232	46	Asian	Left fallopian (STIC)	High grade serous carcinoma	High grade	No	pT3c Nx / IIIc
PT-3401	56	White	Left ovary	High grade serous carcinoma	High grade	No	pT3c Nx Mx/ IIIc
PT-6885	66	Black	Left fallopian (STIC)	High grade serous carcinoma	High grade	Yes	ypT3c N1a / yIIIc
PT-5150	62	White	undetermined	Serous	Not applicable	Yes	ypT3a Nx M1/ Ivb
PT-2834	66	Asian	Fallopian	Malignant mixed Mullerian tumor	High grade	Yes	ypT3c Nx/ y111c
PT-4806	71	Black	Left fallopian (STIC)	High grade serous carcinoma	High grade	Yes	pT3c, N1, M1/ IIIc

Table 1. De-identified patient meta-data for all metastatic ovarian cancer tissues collected from the omentum.

	Gene Cutoff	No of Genes	No of Cells
PT-5150	600	24776	1244
PT-3401	800	32024	3451
PT-6885	800	24063	1071
PT-3232	700	19297	1102
PT-4806	700	26499	1108
PT-2834	800	26221	1909

Table 2. Filter parameters applied to samples collected from six patients and the resulting number of cells and genes per sample.